2021-06

On the Accuracy of an Analytical Solution to Model Wave-Induced Loads on an Underwater Vehicle in Real-Time

Klamo, Joseph T.; Turner, Travis M.; Cool, Colin Y.; Yeager, Kathryn I.; Kwon, Young W.

ASME

Klamo, Joseph T., et al. "On the Accuracy of an Analytical Solution to Model Wave-Induced Loads on an Underwater Vehicle in Real-Time." Journal of Offshore Mechanics and Arctic Engineering 143.3 (2021): 031202.
http://hdl.handle.net/10945/67408

Joseph T. Klamo[1]
Assistant Professor
Department of Systems Engineering,
Naval Postgraduate School,
Monterey, CA 93943
e-mail: jklamo@nps.edu

Travis M. Turner[2]
Department of Systems Engineering,
Naval Postgraduate School,
Monterey, CA 93943
e-mail: travis.turner@ddg111.navy.mil

Colin Y. Cool
Department of Systems Engineering,
University of Virginia,
Charlottesville, VA 22904
e-mail: cyc3va@virginia.edu

Kathryn I. Yeager[3]
York School,
Monterey, CA 93940
e-mail: kathryn.yeager@yale.edu

Young W. Kwon
Distinguished Professor
Fellow ASME
Department of Mechanical and
Aerospace Engineering,
Naval Postgraduate School,
Monterey, CA 93943
e-mail: ywkwon@nps.edu

On the Accuracy of an Analytical Solution to Model Wave-Induced Loads on an Underwater Vehicle in Real-Time

The accuracy of an existing analytical solution for modeling the linear, first-order wave-induced loads on a fully submerged body is investigated. The accuracy is assessed for the situation where the underlying theoretical assumptions are met, and the sensitivity of the accuracy to these assumptions is also explored. The accuracy was quantified by comparing the analytical solutions to experimental measurements from a tow tank with wave generation capability. The assessment showed that when all the assumptions are met, the heave and surge forces are predicted quite accurately but the pitch moment is overpredicted. The results also showed that the deeply submerged assumption is met as long as the body does not cause a disruption of the passing wave on the free surface. The slenderness and end face curvature assumptions are also quite relaxed and the curvature assumption only affects the pitch moment accuracy. The most stringent assumption appears to be the body-of-revolution assumption which can cause all three loads to be predicted poorly. The analytical solution appears to be accurate over a large parameter space and could be incorporated as a wave disturbance model into a virtual environment used to develop control and autonomy of unmanned underwater vehicles. [DOI: 10.1115/1.4049119]

Keywords: hydrodynamics, wave mechanics and wave effects

1 Introduction

There is a growing interest to use unmanned underwater vehicles (UUVs) to perform a larger array of tasks for longer periods of time than they currently do. Many of these new operations would require the UUV to operate near the surface or in the littoral regions. These operating locations would introduce external disturbances on the UUV, in the form of wave-induced loads, that must be accounted for by the vehicle's autonomy and control system if the vehicle is going to operate in an efficient and effective manner. The first step in accounting for these loads is being able to predict the magnitude and phasing of them on the underwater vehicle.

Our goal is broader however than simply accurately estimating the wave-induced loads on a submerged body. We seek the *lowest fidelity model that can provide us the necessary level of accuracy* when predicting wave-induced loads as one part of the larger process of developing and implementing control and autonomy algorithms for UUVs. This requires us to incorporate external disturbance models, such as wave-induced load models, into other models that capture the dynamic response, control behavior, and autonomy of the vehicle. Bingham et al. [1] discussed this same trade-off issue between fidelity and accuracy, but as it pertains to the complexity of the dynamic response model used to represent the vehicle, in their case a surface craft.

The simplest model that still provides the required accuracy is the preferred choice not only for the ease of incorporating that model into other models in the system, but also for the speed in which the vehicle behavior can be simulated. The development process is carried out in a complete virtual environment such as the Gazebo robot simulator coupled with the Virtual RobotX (VRX) simulator. Furthermore, if one achieves real-time calculations, then the developed autonomy could be put directly onto the vehicle itself as well.

If we are only concerned with the accuracy of the model, then methods such as direct numerical simulations (DNS), could be employed. A number of studies have used complex computational fluid dynamics (CFD) solvers to predict the wave-induced loads on a submerged body. Using a finite-difference method, Ananthakrishnan and Zhang [2] simulated the surge and heave forces on the Ocean EXplorer (OEX) class of AUVs developed at Florida Atlantic University. Jones et al. [3] did a preliminary assessment of using the high-fidelity computational dynamics code ANSYS CFX to simulate the wave-induced loads on a submerged square cross-sectional body with flat face end faces due to regular waves. Using the CFD code REX, Carrica et al. [4,5] simulated a Joubert BB2 geometry submarine operating near the surface in irregular waves. Although providing the greatest level of fidelity, and presumably accuracy as well, these methods also are the most computationally time intensive and would not be practical to use inside a virtual simulation environment.

A second approach would also be to use computational methods, but ones with a lower level of fidelity, such as potential flow panel methods. Numerous investigations have taken this approach to determine the wave-induced loads on a submerged body. For example, using three-dimensional potential theory, Pinkster [6] studied the

[1]Corresponding author.
[2]Currently an Engineer Officer onboard USS *Spruance* (DDG-111) at Naval Base San Diego, CA.
[3]Currently an undergraduate student at Yale University, New Haven, CT.

Contributed by the Ocean, Offshore, and Arctic Engineering Division of ASME for publication in the JOURNAL OF OFFSHORE MECHANICS AND ARCTIC ENGINEERING. Manuscript received August 23, 2019; final manuscript received November 5, 2020; published online March 16, 2021. Assoc. Editor: Felice Arena.

nonlinear, second-order mean forces and moments on a circular cylinder in regular waves. Crook [7] also simulated the nonlinear mean loads on a submerged body under a regular wave using a source panel method. Panel methods contain a reasonable level of fidelity, capturing both diffraction and radiation effects, and when implemented on modern computers, run very efficiently. They could potentially be incorporated into the virtual simulation environment as part of the vehicle autonomy development process. However, to deploy autonomy to an actual vehicle requires that the models run real time, and panel methods are typically not capable of this.

A final approach would be to use an analytic solution for predicting wave-induced loads. This would be capable of running real time but would provide a low-level of fidelity and potentially not the required accuracy. A number of theoretical studies have developed expressions for the forces and moments on a submerged body under waves. Some of the earliest theoretical work was done by Dean [8] and Ursell [9,10]. They each developed analytical solutions for the linear, first-order loads on a fixed circle submerged under a regular wave. Ogilvie [11] extended this work to include the nonlinear, second-order mean forces and Arena [12] noted a missing term in the formulation.

A major practical limitation of these efforts, however, was that they were only solving the two-dimensional problem. Therefore, they are not useful for our goal unless generalized to three-dimensional results. Later, Cummins [13] deduced the linear, first-order forces and moments experienced by a slender body-of-revolution submerged beneath a regular wave, solving the three-dimensional problem. Subsequently, Newman [14] and Lee and Newman [15] determined theoretical approximations for the nonlinear, second-order mean heave force and pitch moment for a submerged body without forward speed subjected to a regular wave. Wilmott [16], using a different approach, also theoretically derived the nonlinear, second-order mean heave force on a deeply submerged slender body-of-revolution in a regular wave for a head seas orientation with forward speed.

There are two main drawbacks for using an analytic solution with a low-level of fidelity. The first is that multiple analytic results will have to be used to capture all the various hydrodynamic effects. For instance, only the first-order, linear, incident wave forces can be predicted using the result from Cummins. To predict the nonlinear, mean wave-induced loads that result from wave diffraction, or the low-frequency loads from multiple wave interactions, will require using additional solutions. However, this is straightforward to overcome by simply combining models that each capture an important aspect of the physics. The second drawback is that the analytic solution may not have the required level of accuracy to be useful in its intended purpose. If this is the case, then the only solution is to go to a higher fidelity model.

A shortcoming of much of the previous theoretical work is that the accuracy of the predictions are unknown. The limited amount of available experimental results in the open literature for comparison makes such an endeavor difficult. Cummins [17] compared his theoretical results to experiments that were conducted at Stevens Institute. However, he noted that there was large experimental scatter in the data and that in many cases differences from the theory are less than the data scatter. An early experimental effort by Henry et al. [18] produced results of unknown quality due to large structural vibrations in the setup and a large uncertainty on the measured wave heights. More recently, an experimental study by Khalil [19] measured the nonlinear mean forces on a circular and square cross-sectional cylinder. Finally, Turner et al. [20] and Whitmer et al. [21] both experimentally measured the linear forces and moments on a circular cylinder with hemispheric end caps due to a single regular wave at various frequencies. The latter study also included two-component wave fields to create and measure the low-frequency nonlinear loads on the body.

Therefore, the objectives of this study are to determine the accuracy of an analytical solution capable of real-time prediction of the linear, first-order wave-induced loads on a submerged vehicle, not only when the underlying theoretical assumptions are satisfied but also to explore the sensitivity of the accuracy of the solution when these assumptions are not met. This is important because there is not a single universal shape for a UUV and each one potentially satisfies a different number of assumptions in the underlying theory. This will allow us to understand the accuracy of our analytic model for different UUV hull shapes.

To be consistent with the assumptions of our theoretical model, a large "fineness" ratio body-of-revolution with minimal end face curvature was utilized. This geometry was a circular cylinder with hemispheric end caps and a length-to-diameter ratio, or slenderness, of ten. To further be consistent with the theoretic assumptions, this geometry was tested deeply submerged and the loads on the body were measured experimentally and compared to the analytical solution results. Then, the limits of these assumptions were explored by decreasing the depth of submergence, decreasing the body slenderness, using a non-body-of-revolution geometry, and having an infinite curvature end cap. The "fineness" ratio, or slenderness, was decreased by decreasing the length of the body by half. The body-of-revolution was violated by using a square cross-section geometry. Finally, curvature of the end cap was increased by replacing the hemispheric end cap on the circular geometry with a flat circular plate. The loads on the altered geometries were also experimentally measured and compared to the analytical results to quantify the significance of the various assumptions.

2 Theoretical Derivation

Cummins [13] undertook a theoretical study to derive expressions for the hydrodynamic loads experienced by a submerged vehicle moving under a regular wave. To make an analytical solution possible, he made a number of assumptions:

(1) the vehicle is in a potential, inviscid flow;
(2) the geometry of the vehicle is a body-of-revolution;
(3) the "fineness," or slenderness, of the vehicle must be large;
(4) the wavelength to vehicle diameter must be large;
(5) the vehicle is deeply submerged;
(6) the vehicle ends must not have too high of curvature;
(7) the vehicle is traveling parallel to the free surface; and
(8) the vehicle has a constant velocity.

The first assumption is required to avoid the complexities caused by viscosity and reduces the problem to solving the Laplace equation. The body-of-revolution assumption arises from placing singularities along the axis of the body to meet boundary conditions. The third assumption requires a large vehicle length-to-diameter so that any short body segment can be represented with two-dimensional singularities. The long wavelength relative to vehicle diameter assumption is always met for wave conditions that cause meaningful loading. The fifth assumption exists because the only free surface modification that the theory can capture is the wave generated on a calm water surface by a moving submerged body. The end cap curvature assumption results from simplifications to perform the surface integral for the moment calculation. The seventh assumption requires the vehicle to have no pitch angle while the last assumption eliminates considering the effects of the vehicle accelerating.

This investigation focuses on the potential impacts of the second, third, fifth, and sixth assumptions. The experimental testing was conducted in such a way to eliminate or minimize the potential effects of the other assumptions. The fourth assumption was always met by using wavelengths that were five vehicle diameters in length or longer. The seventh assumption was dealt with by always having the body at a pitch angle of approximately 0 deg. The first and eighth assumption were addressed by testing the body at zero speed. This minimized the impact of testing in a viscous fluid, in violation of assumption one. Testing with forward speed would create a more pronounced boundary layer around the body and a separation region behind it. It also ensured that there was no vehicle accelerations during testing, in violation

of assumption eight. Finally, testing at zero speed eliminates the possibility of any free surface modification due to the *forward movement* of the body. This forces any free surface modifications to be due to the presence of the body itself near the free surface, which the theory does not have the capability to capture.

The generalized equations for the first-order, linear surge force, heave force, and pitch moment on an arbitrary, slender, body-of-revolution submerged under a monochromatic wave was derived by Cummins [13]. For the expressions to be useful, however, the integrals they contain must be evaluated over the length of the body to account for the specific geometry.

Our body selection and testing approach for this investigation simplified the generalized equations of Cummins. The body geometries of interest were all symmetric fore to aft. Also, this investigation only tested zero speed cases and only explored waves propagating along the longitudinal axis of the body. For these constraints, the surge force, F_x, then simplifies to

$$F_x = -\frac{1}{2}\rho g A_o h\left(\frac{\pi}{\lambda^*}\right)\exp\left(-2\pi\frac{d}{\lambda}\right)b_0\cos(\omega_e t) \tag{1}$$

where ρ is the fluid density, g is the gravitational acceleration, A_o is the cross-sectional area of the body at its longitudinal midpoint, h is the wave height, λ^* is the wavelength, λ, nondimensionalized by the overall body length L, d is the centerline depth of the body, b_0 is an integral expression, ω_e is the encounter frequency, and t is time. The heave force, F_z, reduces to

$$F_z = -\rho g A_o h\left(\frac{\pi}{\lambda^*}\right)\exp\left(-2\pi\frac{d}{\lambda}\right)b_0\sin(\omega_e t) \tag{2}$$

which has a similar form to the surge force but is larger by a factor of two. The pitch moment, M_y, simplifies to

$$M_y = \frac{1}{2}\rho g A_o L h\left(\frac{\pi}{\lambda^*}\right)\exp\left(-2\pi\frac{d}{\lambda}\right)a_1\cos(\omega_e t) \tag{3}$$

which is also similar to Eqs. (1) and (2) but contains an extra length term, L, and the integral expression a_1 instead of b_0. Equation (1) through (3) are expressed here in dimensional form and the encounter frequency is denoted as ω_e instead of the ω notation that Cummins uses.

To calculate the loads on the body, the quantities b_0 and a_1 must be evaluated for our particular geometry of interest. It is natural to break the integral involving b_0 into the following three pieces

$$\begin{aligned} b_0 = &\int_{-1}^{-\alpha} L^{*2}\left[(1-\alpha)^2-(\xi+\alpha)^2\right]\cos\left(\frac{\pi}{\lambda^*}\xi\right)d\xi \\ &+\int_{-\alpha}^{\alpha}\cos\left(\frac{\pi}{\lambda^*}\xi\right)d\xi \\ &+\int_{\alpha}^{1} L^{*2}\left[(1-\alpha)^2-(\xi-\alpha)^2\right]\cos\left(\frac{\pi}{\lambda^*}\xi\right)d\xi \end{aligned} \tag{4}$$

where L^* is the length-to-diameter ratio, L/D, ξ is the nondimensional body axis coordinate, $2x/L$, and $\alpha = (L^*-1)/L^*$. The first integral in Eq. (4) corresponds to the stern hemispheric end cap of our circular geometry, the middle integral covers the parallel mid-body portion, and the final integral deals with the bow hemispheric end cap.

The integral for a_1 is also broken up into three pieces in the same manner

$$\begin{aligned} a_1 = &\int_{-1}^{-\alpha} L^{*2}\left[(1-\alpha)^2-(\xi+\alpha)^2\right]\xi\sin\left(\frac{\pi}{\lambda^*}\xi\right)d\xi \\ &+\int_{-\alpha}^{\alpha}\xi\sin\left(\frac{\pi}{\lambda^*}\xi\right)d\xi \\ &+\int_{\alpha}^{1} L^{*2}\left[(1-\alpha)^2-(\xi-\alpha)^2\right]\xi\sin\left(\frac{\pi}{\lambda^*}\xi\right)d\xi \end{aligned} \tag{5}$$

and is identical to Eq. (4) except that $\cos(\cdot)$ is replace by $\xi\sin(\cdot)$.

This effort utilized the web-based Wolfram Alpha to perform the symbolic integration. After some algebraic manipulation, the analysis produced the following expressions for b_0 and a_1

$$\begin{aligned} b_0 = 2L^{*2}\left(\frac{\lambda^*}{\pi}\right)^3\Bigg\{ &-\left[(\alpha-1)^2\left(\frac{\pi}{\lambda^*}\right)^2+2\right]\sin\left(\alpha\frac{\pi}{\lambda^*}\right) \\ &+2\sin\left(\frac{\pi}{\lambda^*}\right)+2(\alpha-1)\frac{\pi}{\lambda^*}\cos\left(\frac{\pi}{\lambda^*}\right)\Bigg\} \\ &+2\left(\frac{\lambda^*}{\pi}\right)\sin\left(\alpha\frac{\pi}{\lambda^*}\right) \end{aligned} \tag{6}$$

$$\begin{aligned} a_1 = 2L^{*2}\left(\frac{\lambda^*}{\pi}\right)^4\Bigg\{ &-\left[(\alpha-1)^2\left(\frac{\pi}{\lambda^*}\right)^2+6\right]\sin\left(\alpha\frac{\pi}{\lambda^*}\right) \\ &+\alpha\frac{\pi}{\lambda^*}\left[(\alpha-1)^2\left(\frac{\pi}{\lambda^*}\right)^2+2\right]\cos\left(\alpha\frac{\pi}{\lambda^*}\right) \\ &+2\left[(\alpha-1)\left(\frac{\pi}{\lambda^*}\right)^2+3\right]\sin\left(\frac{\pi}{\lambda^*}\right) \\ &+2\left(2(\alpha-1)-1\right)\frac{\pi}{\lambda^*}\cos\left(\frac{\pi}{\lambda^*}\right)\Bigg\} \\ &+2\left(\frac{\lambda^*}{\pi}\right)^2\left[\sin\left(\alpha\frac{\pi}{\lambda^*}\right)-\alpha\frac{\pi}{\lambda^*}\cos\left(\alpha\frac{\pi}{\lambda^*}\right)\right] \end{aligned} \tag{7}$$

where the expressions were grouped based on trigonometric terms.

The final complete analytic expressions for the surge and heave forces are obtained by inserting the result from Eq. (6) into Eqs. (1) and (2), respectively. In a similar manner, the full analytic expression for the pitch moment is achieved by putting the result from Eq. (7) into Eq. (3). It is important to note that only the general profile of the geometry has been fixed while the actual diameter and length of the body are still variables and captured by the parameters A_o, L^*, and α. Therefore, this analytical solution is able to account for slenderness changes to the body-of-revolution and end cap curvature changes from a hemisphere to a flat plate.

3 Description of Experimental Setup

3.1 Tow Tank and Wavemaker. The experiments were conducted using the tow tank with wave making capability at the Naval Postgraduate School. A brief description of the testing facility is provided here; a more thorough description, along with an image of the tank, is provided in Klamo et al. [22]. The tow tank is 0.914 m (3 ft) wide by 1.219 m (4 ft) deep and has a total length of 10.973 m (36 ft). The water depth is nominally 0.914 m (3 ft). It is constructed from aluminum and contains Plexiglass panels on one side to allow for easy underwater observation of bodies during testing.

The wavemaker is a vertically plunging wedge that is 0.610 m (2 ft) in height with a 35 deg interior angle from the vertical and is slightly shorter than the width of the tank. The wedge is attached to a support frame that oscillates along a pair of vertical rails attached directly to the tow tank. At the opposite end of the tank is a two-layered wave absorbing beach. The two layers are perforated acrylic sheets 1.219 m (4 ft) in length with staggered 9.525 mm (3/8") diameter holes. The sheets are slightly shorter than the width of the tank so a frame holds the two layers together and spans the remaining width. The beach is fixed in place at an inclined angle of roughly 12 deg.

3.2 Description of Body Geometries. The more slender body used for testing was a hollow, free-flooding 11.430-cm (4.5-in.) diameter circular cylinder with hemispheric end caps and a total length of 1.143 m (45 in.). The body used a 1.029-m (40.5-in.) length extruded aluminum tube with a wall thickness of 3.175 mm (1/8")

as the parallel mid-body section. The hemispheric end caps were produced using rapid prototyping and made of polycarbonate. This more slender body had an L^* of 10.

To reduce the slenderness of the body, the extruded aluminum mid-body section was replaced by a 45.720-cm (18-in.) length parallel mid-body made up of two pieces of polycarbonate with a thickness of 3.175 mm (1/8″) that was also produced using rapid prototyping. The same hemispheric end caps were used and produced a total length of 57.150 cm (22.5 in.). This less slender body had an L^* of 5.

The non-body-of-revolution body was a free-flooding 10.160-cm (4-in.) sided square cross-sectional geometry. More and less slender bodies were constructed in an identical method as for the circular body. The longer body used an extruded aluminum mid-body and the shorter one used two polycarbonate pieces. The thickness was the same as with the circular body as well. The end caps for the square geometry were half circular cylinders to capture the same curvature as a hemisphere but still align with cross-section of the mid-body.

The body for testing the end cap curvature was created by replacing the hemispheric end caps on the circular geometry bodies with circular flat end plates. The plates were fabricated using rapid prototyping and made from polycarbonate as well. All rapid prototyping was performed on a Fortus 400mc 3D printer. Figure 1 shows a sample of all three body configurations tested.

No alteration to the extruded aluminum or as-printed polycarbonate surface finish was undertaken. Besides the tiny gaps where the end caps and mid-body pieces met, the only other surface feature on the bodies was a series of bleed holes located along the length of each body and spaced at 90 deg intervals around the circumference. The bleed holes were 3.175 mm (1/8") diameter and ensured that no air was trapped in the body after submerging it.

The size of the bodies tested was selected to ensure that blockage and wall effects did not affect the measured wave-induced loads when the body was fully submerged. The geometry used in this investigation had a tank width to body diameter ratio, W/D, of eight. A set of our experimental measurements were compared to the wave-induced loads measured on a fully-submerged body with a diameter of 15.240 cm (6 in.) which has a W/D of six. Since the bodies were different sizes, the loads and testing parameters must be nondimensionalized appropriately to be compared. This investigation found that the measured nondimensional force and moment coefficients for each of the bodies was consistent across all of our testing conditions. If wall effects were present for a $W/D = 8$ body then we would anticipate that they would be even more pronounced on a $W/D = 6$ geometry. However, since the results were consistent, the analysis showed that blockage and wall effects did not influence our results.

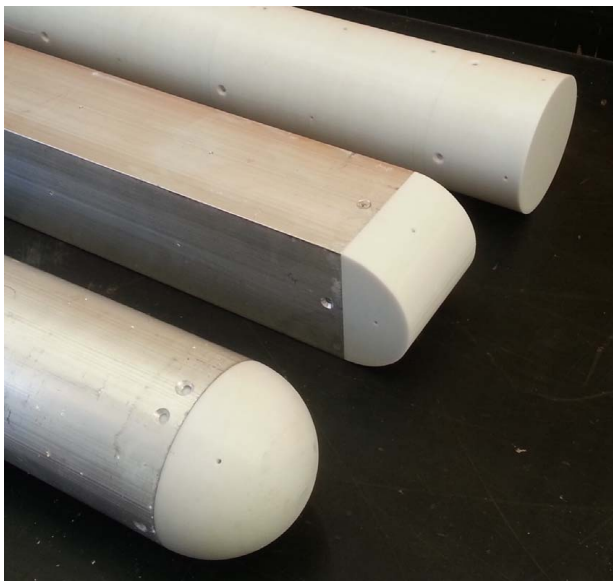

Fig. 1 Picture of the three body configurations tested: circular cylinder with hemispheric end cap (left), square cylinder with half cylinder end cap (middle), and circular cylinder with flat end face (right)

3.3 Test Fixture. A sting style test fixture held each body fixed during testing. Figure 2(*a*) shows an image of the test fixture with the longer circular body attached. Figure 2(*b*) is a schematic that shows the location of the body origin, the orientation of the coordinate axes, and the direction of wave propagation. The horizontal portion of the sting had a length of roughly 16.510 cm (6.5 in.) and consisted of a 3.175-mm (1/8″) thick aluminum tube with an outer diameter of 3.175 cm (1.25 in.). The vertical portion of the sting consisted of a 3.810-cm by 2.540-cm (1.5-in. by 1.0-in.) rectangular anodized aluminum bar 1.054-m (41.5-in.) long that had depth location holes drilled every 2.540 cm (1 in.). The vertical bar was attached to a machined aluminum U-channel using two L-brackets. The U-channel mounted to a load cell that was located above the centerline of the body at its longitudinal midpoint. The other side of the load cell was attached to a stationary frame that was positioned above the tank.

3.4 Instrumentation. A single three-axis AMTI MC3A strain gage load cell measured the loads on the test fixture and body. The excitation voltage and gain of each channel of the load cell can be

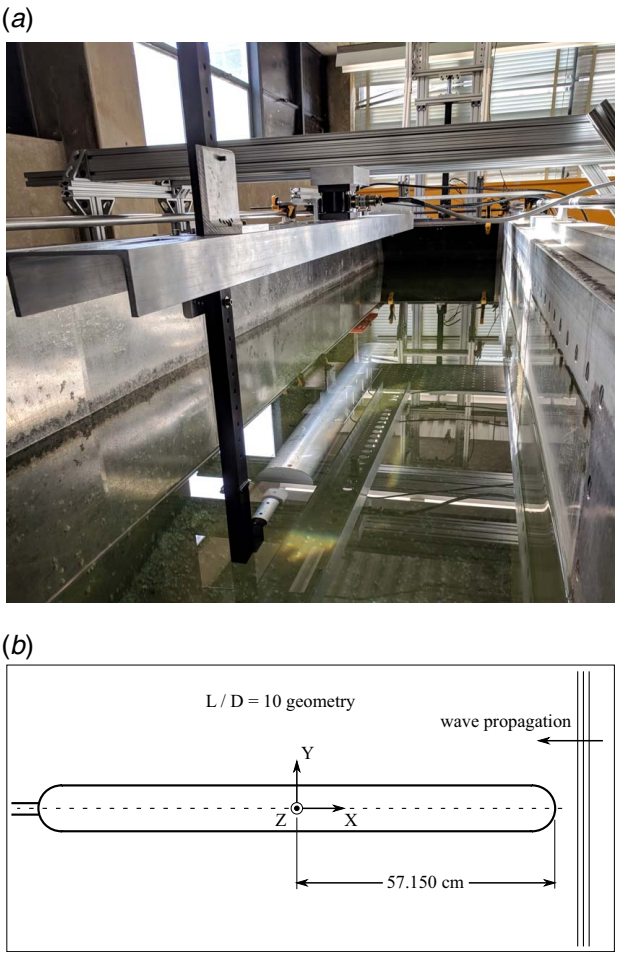

Fig. 2 Overview of the experimental setup: (*a*) photo showing a perspective view of the setup including the tow tank, wavemaker, test fixture, and body and (*b*) schematic of the setup, when looking down from above, showing the body origin location, coordinate system, and wave propagation direction

set independently. The six channels were set to obtain the highest resolution and signal-to-noise ratio while maintaining the required measurement range. An AMTI Gen5 amplifier and signal conditioner handled the independent channel settings of the load cell and fully conditioned the analog output voltage to include compensation for the effects of the cable length. Sample force and moment time histories along with the corresponding frequency content of the signals can be found in Turner et al. [20].

Before testing, the accuracy of the load cell was examined using in-situ verification measurements of steady loads as described in Turner et al. [20]. The uncertainty on the heave force was estimated at 0.89 N (0.2 lbs) while the uncertainty in the pitch moment was 0.28 N-m (2.5 in-lbs). These values represent the minimum measurement uncertainties since they correspond to ideal static conditions while measuring a constant load. During actual testing, the measured loads were dynamic, and the uncertainties are assumed to be slightly larger and better captured by considering the variability in repeated, and neighboring, runs.

The water elevation at four locations along the tank was measured by Senix ToughSonic 14 ultrasonic probes. The probes were located along the centerline of the tank approximately 29.210 cm (11.5 in.) above the calm water surface. In order to measure the incoming wave profile, three probes were located ahead of the bow of the body. The other probe was located 15.240 cm (6 in.) ahead of the midpoint of the body. This allowed for a measurement of any potential wave elevation alterations as waves passed over the body.

All the analog output voltages from the load cell and ultrasonic probes were routed into a single National Instruments data acquisition board (USB-6363, X Series) and sampled at a rate of 50 Hz. The data were collected on a laptop computer (Dell Precision 17 7000 Series) through a USB connection. The collection software was a custom-written MATLAB script using the data acquisition toolbox functions.

3.5 Test Conditions. For this investigation, the body had zero forward speed and was therefore stationary for all the runs. Four centerline depths, d, of the body were examined. These centerline depths were 11.430, 17.145, 22.860, and 34.290 cm (4.50, 6.75, 9.00, and 13.5 in.) and corresponded to nondimensional depths, $d^* = d/D$, of 1.0, 1.5, 2.0, and 3.0, respectively, where D is the diameter of the body. The cross-sectional area of the square body was specifically chosen to match the area of the circular body. This made the "equivalent diameter" of the square body, based on area, equal to the diameter of the circular bodies. The desired pitch angle of the body was 0 deg but when attached to the sting, a slight downward pitch angle of roughly 0.08 deg was routinely measured. The desired yaw angle of the body was also 0 deg. A slight yaw of roughly 0.1 deg toward port was also measured.

A single wave height of 5.080 cm (2 in.) was used throughout the study. Prior to testing, the required wavemaker input signal, to generate a wave of this height at each of the various wavelengths of interest, was determined experimentally. The wave elevation was measured without the body present using the probe located 15.240 cm ahead of where the midpoint of the body would be when it was present later during testing. Each wave was generated multiple times, and its wave height checked, to ensure that the wavemaker generated a repeatable wave for each input signal.

The height of the incoming wave was measured real time during each test run by the three probes ahead of the body. After a test run, the wave height for that run was calculated using the recorded wave elevation time history from these wave probes to ensure the desired wave height was achieved. Figure 3 shows the distribution of the mean wave height from these three probes for various test conditions. The figure contains the results for each depth tested of the long and short circular body with hemispheric end caps. The wave height distributions demonstrate that the wave environment was consistent for all test runs using these two bodies. The wave height distributions for the achieved wave environments for the other test configurations were also consistent with these results and are not shown individually. The overall mean wave height for all eight test configurations shown was approximately 5.00 cm (1.97 in.), which is only slightly below the desired 5.080 cm value. Assuming a normal distribution of wave heights for each test configuration, as suggested by Fig. 3, then 95% of the mean wave heights fell between ±0.500 cm (±0.197 in.) of the overall mean.

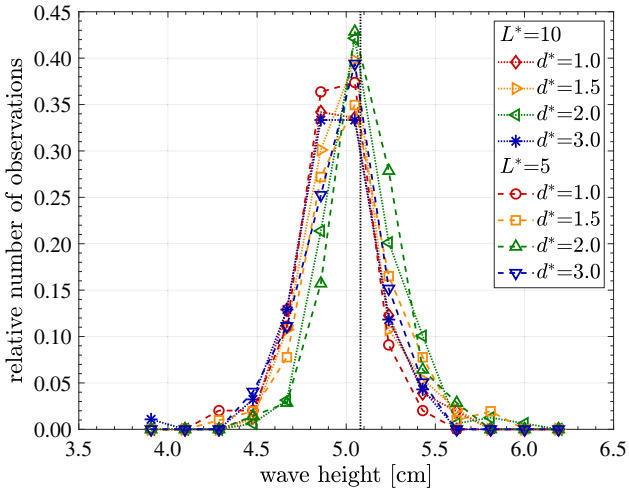

Fig. 3 Summary of the achieved mean wave heights, as measured by the three probes ahead of the body, during testing of the circular geometry with hemispheric end caps

Thirty different wave frequencies, from 0.82 to 1.73 Hz, were used during testing. This frequency range represented the capability range of the wavemaker for the desired wave height. For the longer bodies, these wave frequencies corresponded to a λ^* range of 0.5–2.0 and for the shorter bodies a range of 1.0–4.0. During testing, our analysis found that a small frequency range excited the test rig structure and caused a large amount of variability in the data collected. For the longer body, this occurred for frequencies between 1.296 to 1.227 Hz which corresponded to a λ^* of 0.81 to 0.91. For the shorter body, this occurred for frequencies between 1.404 and 1.265 Hz which corresponded to a λ^* of 1.43 to 1.75. Much of the data for these frequencies was not considered in the analysis.

To estimate the effects of the sting on the measured data, once testing on the bodies was complete, the same wave conditions and submergence depths were repeated with just the sting test fixture in the tank. This data set was used to determine the amplitude and phase, relative to the incoming wave, of the loads from the sting.

4 Description of Data Reduction

The wavenumber, k, for each wave generated was estimated using the finite depth, third-order dispersion relationship

$$\omega^2 = gk\varphi\left(1 + \frac{9 - 10\varphi^2 + 9\varphi^4}{8\varphi^4}(ka_w)^2\right) \tag{8}$$

where ω is the angular wave frequency, which was the same as the wedge oscillation frequency, $\varphi = \tanh(kH)$, H is the water depth, and a_w is the wave amplitude. The wavelength was then estimated as $\lambda = 2\pi/k$. At this point in the data reduction process, the software had not estimated the achieved wave height so the desired wave amplitude of 2.540 cm (1 in.) was used in the calculation. If the 95% bounds of achieved wave heights shown in Fig. 3 had been used in Eq. (8) instead of the desired value, then the wavelengths only change by a maximum of 0.1% for the longest wave and 1.4% for the shortest. The finite depth, third-order dispersion relationship was used instead of the simpler linear dispersion relationship since the waves were quite steep for certain conditions and slightly longer than twice the tank depth for others. For our high

frequencies, between 1.50 and 1.73 Hz, the linear dispersion relationship predicts a shorter wavelength than the finite depth, third-order relationship by 5%–7%.

Each wave elevation time history signal, $\eta(x, t)$, was fit in a least-squares sense to the functional relationship

$$\eta(x, t) = A_1 \cos(kx - \omega t) + B_1 \sin(kx - \omega t) + C \tag{9}$$

where A_1 and B_1 are the cosine and sine components of the first-order amplitude, k is the estimated wavenumber from Eq. (8), x is the probe location in the body coordinate system, and C is the wave elevation, and sensor electrical, offset. The cosine and sine components A_1 and B_1 were converted to an amplitude and phase formulation using trigonometric identities to estimate the wave amplitude, a_w, and wave phase angle, ϕ_w. The importance of including the spatial dependence in Eq. (9) is that all four of the measured wave phases are then based on the same coordinate system, with $x = 0$ at the body origin, and should therefore be equal. This allowed us to estimate the phase of the incoming wave by calculating a mean using the phase values from the three probes that were located ahead of the body.

The wave height, h, was estimated for each wave elevation signal using

$$h = 2a_w\left(1 + \frac{3}{8}(ka_w)^2\right) \tag{10}$$

which is the third-order Stokes wave height approximation. This approximation was used instead of simply twice the wave amplitude since some of the shorter wavelengths tested were quite steep. Klamo et al. [22] showed that the elevation time history of these steep waves in the tow tank are approximated very well by this approximation. For our highest test frequencies, between 1.50 and 1.73 Hz, twice the wave amplitude underpredicts the wave height by 1% to 2%.

Before determining the amplitude and phase of the load channels, the effects of the sting needed to be removed from the as-measured forces and moments. The results from the sting-only testing were used to determine the force and moment amplitudes caused by the sting and the phase that they occur at relative to the incoming wave. The underlying assumption for our sting correction is that the sting and body forces can be superimposed. Strictly speaking, this is not the case since the presence of the body will alter the flow around the sting compared to the sting-only tests. However, previous testing with different sized stings, and even a fairing over the sting, have shown that this assumption is reasonable and does not influence our overall level of uncertainty.

The body surge force, $F_{x,B}(t)$, and heave force, $F_{z,B}(t)$, time histories were then calculated using

$$\begin{aligned} F_{x,B}(t) &= F_{x,L}(t) - a_{F_x,S}\sin(-\omega t + \phi_{F_x,S|w} + \phi_w) \\ F_{z,B}(t) &= F_{z,L}(t) - a_{F_z,S}\sin(-\omega t + \phi_{F_z,S|w} + \phi_w) \end{aligned} \tag{11}$$

where $F_{x,L}(t)$ and $F_{z,L}(t)$ are the load cell as-measured surge and heave force time histories, $a_{F_x,S}$ and $a_{F_z,S}$ are the sting surge and heave force amplitudes, and $\phi_{F_x,S|w}$ and $\phi_{F_z,S|w}$ are the sting surge and heave force phases relative to the incoming wave phase, respectively. For the forces and moments, the body coordinate system, shown in Fig. 2(*b*), is defined with the origin at the center of buoyancy of the geometry with the positive x-axis toward the bow, the positive y-axis toward port, and the positive z-axis pointing upward opposite gravity.

Besides needing to have the sting effects removed, since the load cell was located above the body, the as-measured pitch moment also needs to be moved from the load cell origin to the body origin. The body pitch moment time history, $M_{y,B}(t)$, was calculated using

$$\begin{aligned} M_{y,B}(t) = M_{y,L}(t) &- a_{M_y,S}\sin(-\omega t + \phi_{M_y,S|w} + \phi_w) \\ &- \ell\, a_{F_x,B}\sin(-\omega t + \phi_{F_x,B|w} + \phi_w) \end{aligned} \tag{12}$$

where $M_{y,L}(t)$ is the as-measured pitch moment, $a_{M_y,S}$ is the pitch moment amplitude of the sting, $\phi_{M_y,S|w}$ is the pitch moment phase of the sting relative to the incoming wave, ℓ is the z-component of the position vector pointing from the load cell origin to the body origin, and $a_{F_x,B}$ and $\phi_{F_x,B|w}$ are the amplitude and phase of the body surge force, respectively.

To estimate the amplitude and phase of the body forces, $F_{x,B}(t)$ and $F_{z,B}(t)$, and pitch moment, $M_{y,B}(t)$, the sting-corrected body time history data from Eqs. (11) and (12) were fit in a least-squares sense to the functional relationship

$$\begin{aligned} f(x = 0, t) = A_1 &\cos(-\omega t) + B_1 \sin(-\omega t) \\ &+ A_2 \cos(-2\omega t) + B_2 \sin(-2\omega t) + C \end{aligned} \tag{13}$$

where A_2 and B_2 are the cosine and sine components of the nonlinear double frequency terms, respectively. For the body sizes tested, the nonlinear terms corresponding to the 2ω frequency were small and are not accounted for by the linear theory. The spatial dependence for the load cell channels is absent in Eq. (13) since the load cell is at $x = 0$ in the body coordinate system.

The cosine and sine portions of the first-order load amplitudes were then combined into body force and moment amplitudes, $a_{F_x,B}$, $a_{F_z,B}$, and $a_{M_y,B}$, as well as the corresponding phase angles, $\phi_{F_x,B}$, $\phi_{F_z,B}$, and $\phi_{M_y,B}$ relative to the incoming wave. Since Eq. (12) contains the sting-corrected body surge force amplitude and phase, which was only known after performing the calculation of Eq. (13), the force and moment sting correction could not be done simultaneously. Instead, the surge and heave force time histories were corrected for sting effects using Eq. (11) and then the amplitude and phase of the body surge and heave forces were determined using Eq. (13). Then, the pitch moment time history correction for sting effects could be performed using Eq. (12) followed by the amplitude and phase of the body pitch moment being estimated using Eq. (13) again.

Finally, the body force and moment amplitudes were nondimensionalized by

$$C_{F_x} = \frac{a_{F_x,B}}{\rho g A_o h}, \quad C_{F_z} = \frac{a_{F_z,B}}{\rho g A_o h}, \quad C_M = \frac{a_{M_y,B}}{\rho g A_o h L} \tag{14}$$

which follow naturally from nondimensionalizing Eqs. (1)–(3).

5 Results and Discussion

5.1 Deep Submergence and Slenderness Assumptions. Figure 4(*a*) shows the amplitude of the first-order heave force coefficient comparison between the experimental results and analytical solutions for the more slender, length-to-diameter of ten, body. The comparison is shown over a range of nondimensional wavelengths and at four different centerline depths. The different depths allow us to explore the importance of the deep submergence assumption. Figure 4(*b*) shows the results for the less slender body with a length-to-diameter ratio of 5. The two different body lengths allow us to explore the importance of the slenderness assumption.

In Figs. 4(*a*) and 4(*b*), the solid lines are the analytical solutions of the heave force from Eqs. (2) and (6) using the appropriate values of L^* and α for the two different bodies. The data symbols in the figures represent the experimental results and the dotted and dashed lines are curves fits to those results. The same color is used for matching theoretical and experimental results and each color represents a different depth. The functional relationship used for fitting the nondimensional force data was

$$\begin{aligned} C_F = L^{*2}\exp\left(-2\pi c_1 \frac{d/L}{\lambda^*}\right)\Bigg[c_2\left(\frac{\lambda^*}{\pi}\right)^2 \sin\left(\alpha\frac{\pi}{\lambda^*}\right) \\ + c_3\left(\frac{\lambda^*}{\pi}\right)^2 \sin\left(\frac{\pi}{\lambda^*}\right) + c_4\left(\frac{\lambda^*}{\pi}\right)\cos\left(\frac{\pi}{\lambda^*}\right)\Bigg] \end{aligned} \tag{15}$$

where c_1 through c_4 are the fitting coefficients determined using the curve-fitting toolbox in MATLAB with the initial values being

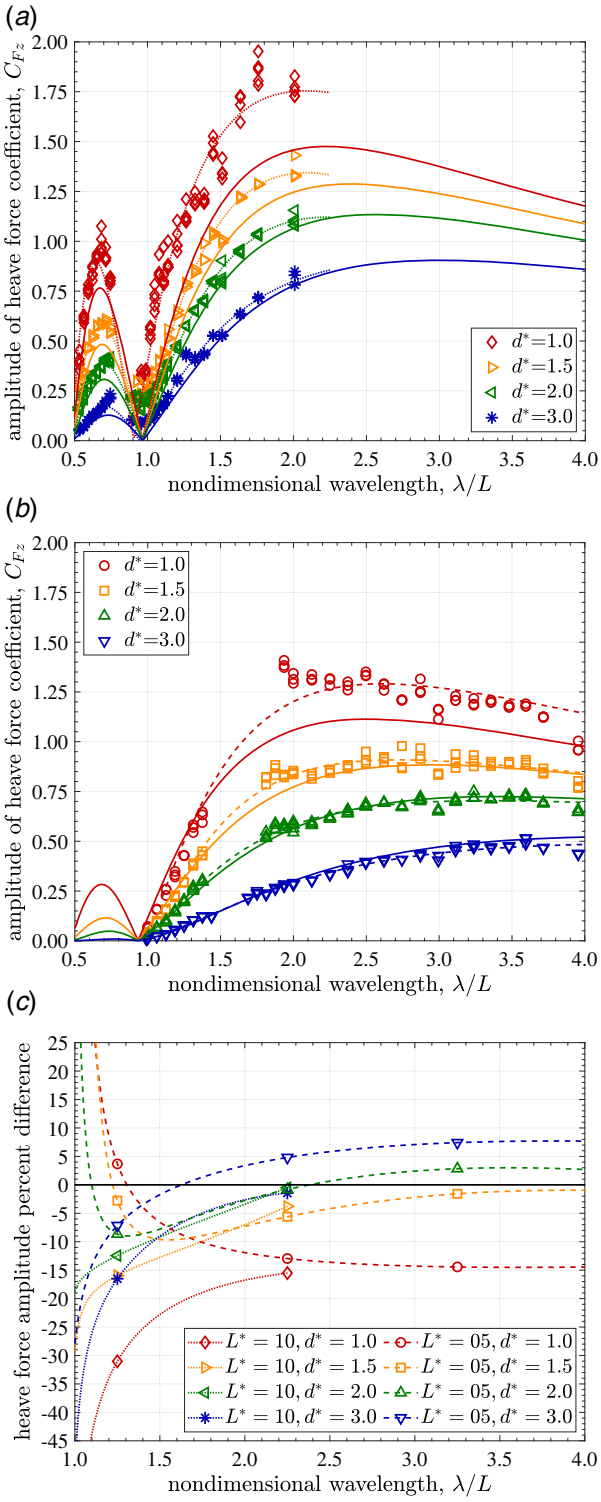

Fig. 4 Heave force amplitude comparison for the circular body with hemispheric end caps over a range of wavelengths, for two different body lengths, and four depths: (*a*) experimental and theoretical results for $L^* = 10$ body, (*b*) experimental and theoretical results for $L^* = 5$ body, and (c) percent difference between theoretical and experimental results

provided by the coefficients in Eq. (6). Equation (15) is a general form of Eqs. (1) or (2) combined with Eq. (6).

Figures 4(*a*) and 4(*b*) show that for longer wavelengths, as long as the body is not extremely shallow, the analytical solution is an accurate model regardless of the body slenderness. The requirement on wavelength appears to be nondimensional wavelengths greater than 2.0. The results also suggest that nondimensional depths greater than 1.0 can be considered submerged enough to use the analytical solution. Furthermore, the figures show that for nondimensional wavelengths less than 1.5, the analytical solution accuracy decreases as wavelength decreases and does not match the experimental results.

For the shallowest depth tested, the analytical solution does not agree with the experimental results regardless of wavelength. We hypothesize that this is due to a wave-body interaction effect that disturbs the free surface structure as the wave passes over the submerged body. Turner et al. [20] showed images of a wave front cleanly passing over a body for $d^* = 2.0$, but for $d^* = 1.0$, the wave breaks as it passes over the extremely shallow submerged body and causes transverse waves to form. The interaction of these transverse waves with the narrow walls of the tank and the sting could potentially be adding to the severity of the disagreement. Regardless, the analytical solution assumes a sinusoidal wave passes over the body and can not capture any changes to the free surface. Therefore, it is not surprising that any operating depth that disrupts the free surface results in the analytical solution poorly modeling the heave force.

Figure 4(*c*) provides a quantitative assessment of the accuracy of the analytical solution by considering the percent difference. The percent difference is defined as the analytical solution minus the experimental measurements and then that difference divided by the experimental measurements. The dotted lines in this figure correspond to the more slender, $L^* = 10$, body while the dashed lines represent the less slender, $L^* = 5$, geometry. For nondimensional wavelengths less that 1.25, the percent difference rapidly diverges due to dividing by very small heave force values. For this reason, this study will mostly be interested in wavelengths greater than 1.5. An important observation is that the accuracy of the analytical solution does vary across the nondimensional wavelengths tested.

For nondimensional wavelengths greater than 1.5, the analytical solution provides an accuracy of ±5% when the body is not in an extremely shallow condition regardless of how slender the body. For the more slender, $L^* = 10$, body, the results end at a nondimensional wavelength of 2.0. However, it appears that the percent difference results are in general agreement with the less slender, $L^* = 5$, body for $1.5 < \lambda/L < 2.0$. This suggests that it is reasonable to assume that our $L^* = 10$ geometry would also show good agreement with the analytical solution for longer wavelengths. For the less slender body at $d^* = 3.0$, as wavelength increases the percent difference does grow slightly larger than +5%. However, the data as a whole suggests this is due to the fact that this condition has the smallest forces and therefore have a slightly larger uncertainty. The more slender body, at the same depth, experiences larger heave forces and the percent difference with the analytical solution is within the ±5% range. Figure 4(*c*) also shows that the consequence of the wave-body interaction and disrupted free surface from extremely shallow operation is that the analytical solution underpredicts the heave force on the body by around −15%. This is true regardless of the slenderness of the body.

Figure 5(*a*) shows the first-order surge force coefficient amplitude comparison to the analytical solution for the more slender body over a range of nondimensional wavelengths and for multiple depths. Figure 5(*b*) contains the results for the reduced slenderness geometry. Figure 5(*c*) shows the percent difference between the analytical solutions and the experimental results for surge force. The formatting in the figures is the same as Fig. 4.

For the surge force, the theory appears to achieve the same level of accuracy as for the heave force provided the wavelengths are, again, long enough. Also similar to the heave force, the figures show that for nondimensional wavelengths less than 1.5, the analytical solution does not agree with the experimental results. The analytical solution appears to overpredict the surge force.

For the less slender, $L^* = 5$, geometry, Fig. 5(*b*) shows that the analytical solution agrees well with the experimental results for

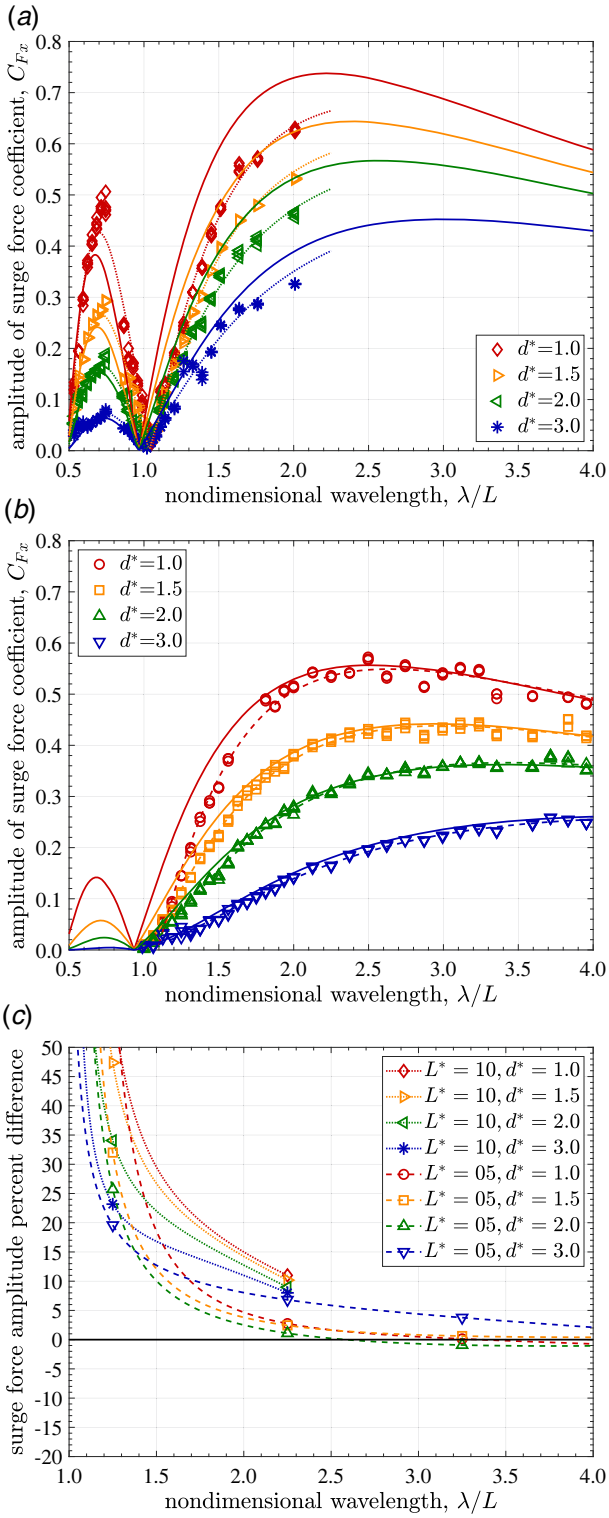

Fig. 5 Surge force amplitude comparison for the circular body with hemispheric end caps over a range of wavelengths, for two different body lengths, and four depths: (*a*) experimental and theoretical results for $L^* = 10$ body, (*b*) experimental and theoretical results for $L^* = 5$ body, and (*c*) percent difference between theoretical and experimental results

all depths tested for nondimensional wavelengths greater than 2.0. Figure 5(*c*) shows that for this geometry, the percent difference between the results is again ±5% in this range. It is interesting that even the very shallow case of $d^* = 1$ showed good agreement. This suggests that the disruption of the free surface causes the vertical pressure profile along the length of the body to change but not the magnitude of the pressure difference across the bow and stern faces of the body.

For the more slender, $L^* = 10$, geometry, Fig. 5(*a*) shows that the analytical solution is approaching the experimental results as wavelength increases but not as quickly as the less slender geometry. Figure 5(*c*) shows the percent difference at a nondimensional wavelength of 2.0 is around +10% to +15% percent. However, it does appear that the percent difference is decreasing and could reach the same level as accuracy as the less slender geometry for nondimensional wavelengths beyond 3.0. Unfortunately, the analysis is forced to extrapolate the $L^* = 10$ geometry results since, due to the facility limitations, this study was not able to test at longer wavelengths. This extrapolation is obviously sensitive to the ending curvature of the curve-fit. One consistency with the less slender geometry is that this geometry also showed that the analytical solution accuracy does not appears dependent on depth, even the extremely shallow test depth.

Finally, the analytical solution is a potential flow solution and therefore does not capture any viscous effects. It is interesting that the disagreement between the results stems from the surge force being overpredicted by the analytical solution. Not accounting for the viscous effects would seem to imply that the theory would underpredict the surge force. Also, the good agreement between the analytical solution and the experimental results at long wavelengths suggests that viscosity has little, if any, effect on the wave-induced surge force, and heave force as well, at zero forward speed. This may not be the case when forward speed is considered with a blunt enough geometry that causes considerable separation over the bow of the vehicle.

Figure 6(*a*) shows the comparison between the theoretically predicted and experimentally measured amplitude of the first-order pitch moment coefficient for the more slender geometry. Figure 6(*b*) shows the results for the smaller length-to-diameter, less slender, geometry. The formatting of the figures is the same as the corresponding heave and surge force figures. The functional relationship for fitting the nondimensional moment was

$$C_M = L^{*2}\exp\left(-2\pi c_1 \frac{d/L}{\lambda^*}\right)\left[c_2\left(\frac{\lambda^*}{\pi}\right)^3 \sin\left(\alpha\frac{\pi}{\lambda^*}\right) + c_3\left(\frac{\lambda^*}{\pi}\right)^2 \cos\left(\alpha\frac{\pi}{\lambda^*}\right) + c_4\left(\frac{\lambda^*}{\pi}\right)\sin\left(\frac{\pi}{\lambda^*}\right) + c_5\left(\frac{\lambda^*}{\pi}\right)^3 \sin\left(\frac{\pi}{\lambda^*}\right) + c_6\left(\frac{\lambda^*}{\pi}\right)^2 \cos\left(\frac{\pi}{\lambda^*}\right)\right] \tag{16}$$

where c_1 through c_6 are another set of fitting coefficients determined using the curve-fitting toolbox in MATLAB with the initial values being provided by the coefficients in Eq. (7). Equation (16) is a general form of Eq. (3) combined with Eq. (7).

Figures 6(*a*) and 6(*b*) show that the analytical solution predicts the pitch moment less accurately than the heave or surge forces. Both figures suggest that the analytical solution overpredicts the pitch moment for both slenderness value geometries and for all depths. This lower accuracy exists despite the high accuracy of the analytical solution at predicting the heave and surge forces. This suggests that although the magnitude of the heave force is reasonably captured by the theory, the distribution of the force along the body is not. An incorrect force distribution, specifically at the end caps, will have the largest effect on the pitch moment due to the moment arm being the largest there. This is consistent with typical strip theory accuracy for forces and moments and is mainly attributed to the mathematical representation of the ends of the geometry that cause issues with the predicted force distributions there.

Figure 6(*c*) contains the percent difference between the analytical solution and the experimental results for the first-order pitch moment amplitude. As nondimensional wavelength decreases less

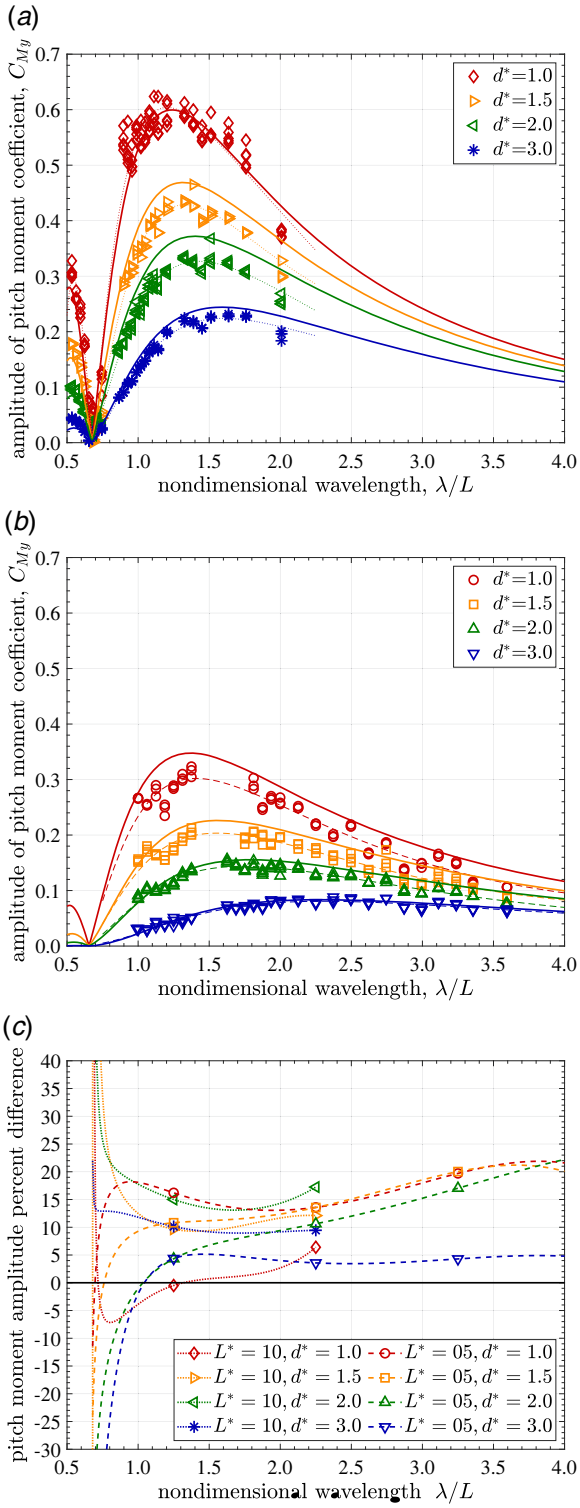

Fig. 6 Pitch moment amplitude comparison for the circular body with hemispheric end caps over a range of wavelengths, for two different body lengths, and four depths: (*a*) experimental and theoretical results for $L^* = 10$ body, (*b*) experimental and theoretical results for $L^* = 5$ body, and (*c*) percent difference between theoretical and experimental results

than 1.0, the percent difference rapidly increases due to the pitch moment being quite small in this region and having a local minimum around a value of 0.6. For nondimensional wavelengths greater than 1.5, it appears that the analytical solution overpredicts the pitch moment amplitudes by between +10% to +20%. There does not appear to be any dependence on depth or the slenderness of the geometry over the ranges tested in this study. The less slender body at a nondimensional depth of 3.0 appears to show a slightly better agreement. However, the data as a whole suggests that this is mainly due to the pitch moment being very small for this condition. For nondimensional wavelengths greater than 3.5, Fig. 6(*c*) shows an increase in the percent difference. However, at these long wavelengths, the pitch moment is very small and therefore the percent difference value is quite sensitive to the actual curvature of the ends of the curve-fit lines. In general, the moment percent difference curves have more fluctuations, or wiggles, than the heave and surge force percent difference curves. This is due to the moment curve-fit function, given by Eq. (16), having more terms and therefore being able to exhibit more local curvature.

The analytical solution for the more slender geometry at the extremely shallow depth, $d^* = 1.0$, was much closer to the experimental results than the other cases. The data suggest that this was due to the actual heave force being larger than the analytical solution which then caused the theory, which normally overpredicts the pitch moment, to artificially predict it more accurately in this case. The wave influence depth, d/λ also appears to play a role, however, since the less slender body at $d^* = 1.0$ did not show this increased pitch moment accuracy even though the heave force was also underpredicted for it. For a given nondimensional wavelength, the more slender body is at a smaller d/λ value than the less slender body meaning it experiences stronger wave influences.

Finally, the pitch moment experimental results do contain the largest uncertainty due to the corrections for both the effects of the sting and of translating the pitch moment origin. This is observed by noting the larger amount of scatter in the experimental results for the pitch moment compared to the heave and surge force results. The fitting of the experimental results to a curve-fit reduces the impact of this uncertainty from the individual experimental data points on the percent difference calculations. For this reason, the less accurate pitch moment predictions are believed to be due more to limitations of the theory assumptions rather than caused by the larger uncertainty in the experimental results.

5.2 Body-of-Revolution Assumption. Although the theory allows for the cross-sectional area of the body to change along its length, it is restricted to being a body-of-revolution and thus always having a circular cross section shape. To explore the importance of this assumption, a body with the same cross-sectional area as the circular body, but with a square cross-sectional shape, was tested and compared to the analytical solution for a *circular* cross section.

Figure 7(*a*) shows the experimentally measured first-order heave force coefficient amplitude for a square cross-sectional body with an $L^* = 5$ compared with the circular cross-sectional analytical solution for the same length-to-diameter body. The experimental results in the figure are denoted with various style data markers. The dashed lines correspond to curve-fits of the experimental data using the functional form given by Eq. (15). The solid lines are the analytical solution, given by Eqs. (2) and (6). This is the same analytical solution from the depth and slenderness study since the theory can not model the square cross-sectional shape. The various colors in the figure correspond to different testing depths.

Figure 7(*a*) indicates that, for nondimensional wavelengths greater than 1.5, the analytical solution underpredicts the heave force on a square body. The accuracy of the analytical solution appears to vary with depth. As the body submerges to a deeper depth, the circular cross-sectional analytical solution is more accurate at predicting the heave force on the square body.

Figure 7(*b*) quantifies the accuracy of the analytical solution by showing the percent difference between the experimental results and analytical solutions. The percent difference is formulated in the same manner as in the depth and slenderness study. The dashed lines correspond to the less slender geometry test results. For nondimensional wavelengths of 1.5 and longer, the analytical solution

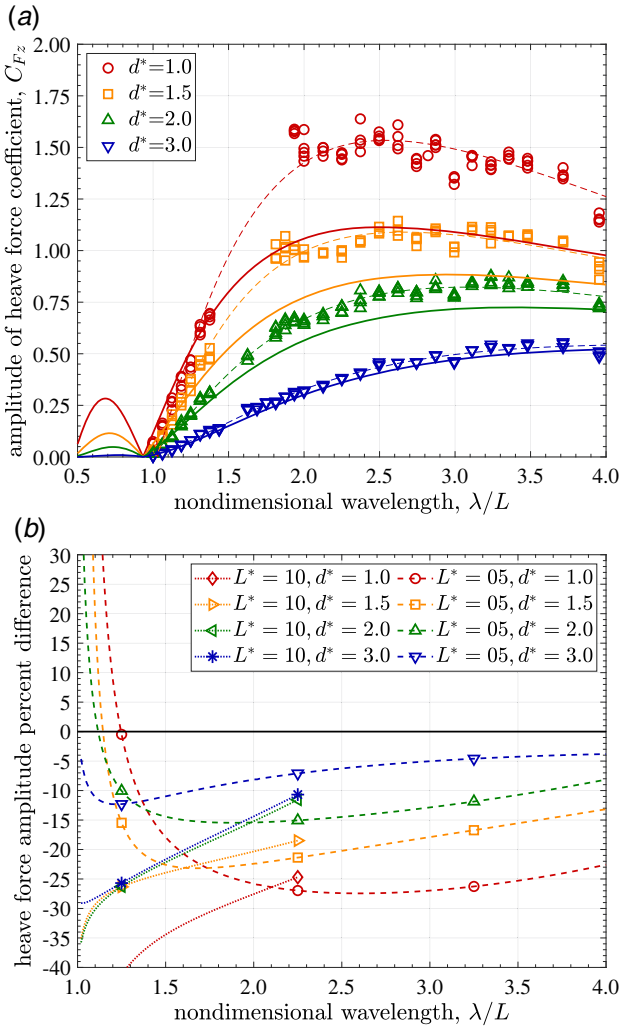

Fig. 7 Heave force amplitude comparison for the square body over a range of wavelengths, for two different body lengths, and four depths: (*a*) experimental and theoretical results for $L^* = 5$ body and (*b*) percent difference between theoretical and experimental results

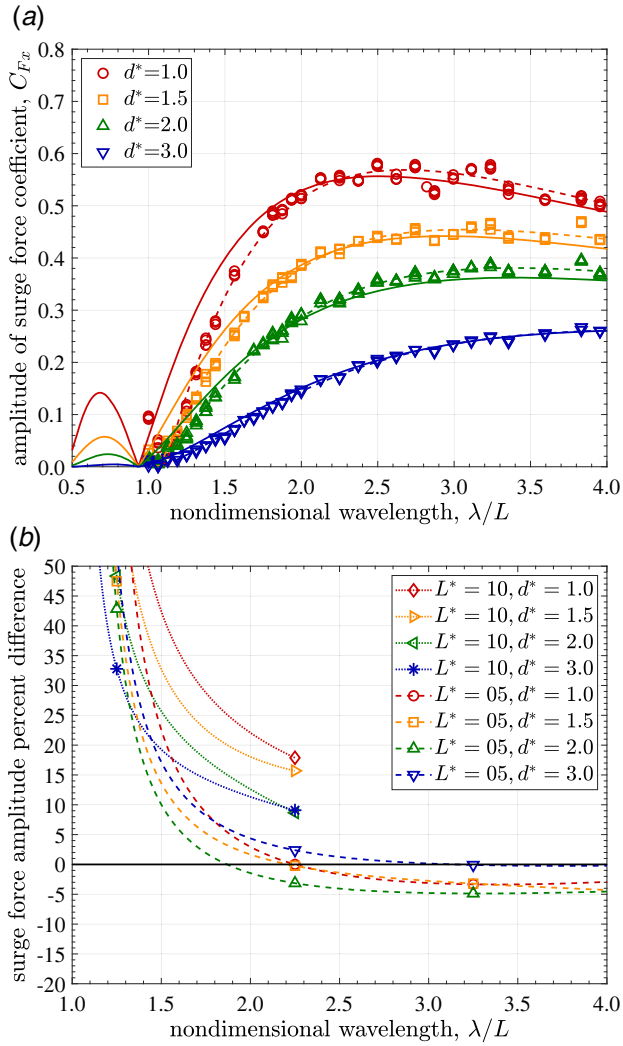

Fig. 8 Surge force amplitude comparison for the square body over a range of wavelengths, for two different body lengths, and four depths: (*a*) experimental and theoretical results for $L^* = 5$ body and (*b*) percent difference between theoretical and experimental results

underpredicts the heave force on a square body by −30% to −20% for a nondimensional depth of 1.0. As the submergence depth increases to $d^* = 2.0$, the solution underpredicts the heave force by −20% to −15%. For the other two submergence depths tested, the solution underpredicts the heave force by −15% to −10% for $d^* = 2.0$ and approximately −10% to −5% for $d^* = 1.0$.

A more slender, $L^* = 10$, square geometry was also experimentally tested and compared to the equivalent analytical solution. The dotted lines in Fig. 7(*b*) represent these results. The more slender body results showed the same general behavior, but over a smaller nondimensional wavelength range. The similarity between the dashed and dotted lines in the figures confirms this.

This study also examined the surge force. Figure 8(*a*) contains both the experimental results and the analytical solutions for the less slender, $L^* = 5$, geometry. The formatting of the figure is the same as in Fig. 7(*a*). Surprisingly, the figure shows that unlike the heave force, the surge force analytical solution for a circular cross section agrees quite well with the experimental results for a square cross section. Since the circular cross-sectional geometry surge force was predicted very accurately by the analytical solution, this suggests that the cross-sectional shape only has a minor effect on the surge force. In our case, a square cross-sectional geometry causes the surge force to increase slightly resulting in the analytical solution now slightly underpredicting the surge force for the square geometry.

Figure 8(*b*) displays the percent difference between the analytical solutions and the experimental results. The dashed line again corresponds to the less slender body results shown in Fig. 8(*a*). The figure shows that for nondimensional wavelength less than 1.5, the analytical solution does not predict the surge force well. However, for nondimensional wavelengths greater than 2.0, the analytical solution is able to predict the surge force within ±5% for all depths tested. For nondimensional wavelengths beyond 2.5, the analytical solution appears to steadily underpredict the surge force slightly, but by less than −5% for all depths tested.

The dotted lines in Fig. 8(*b*) correspond to the more slender, $L^* = 10$, geometry results. These percent difference results show the same general behavior as the less slender geometry results but appear to suggest that the analytical solution is less accurate at predicting the surge force. For example, for nondimensional wavelengths around 2.0, the analytical solution overpredicts the surge force between +10% and +20% compared with the ±5% for the less slender geometry. However, the percent differences appear to be decreasing and for longer wavelengths, the analytical solution may eventually reach that same level of accuracy. This is the same behavior for the $L^* = 10$ geometry, relative to the $L^* = 5$

geometry, that was observed with the surge force depth and slenderness results shown in Fig. 5(*c*).

Figure 9(*a*) contains a comparison between the pitch moment amplitudes of the analytical solutions for a circular cross-section and the experimental results for the square geometry, for a length-to-diameter ratio of 5. The results show that the analytical solution arbitrarily predicts the pitch moment accurately. This results from the fact that the analytical solution overpredicted the pitch moment on the circular cylinder and the square geometry experiences a larger pitch moment than the circular geometry, similar to the larger heave force it also experiences. This increased pitch moment on the square geometry is only slightly less than the amount that the analytical solution overpredicted the pitch moment on the circular body. This results in the analytical solution only slightly overpredicting the pitch moment on the square geometry. Since this good agreement is accidental, it is very likely that this level of accuracy will not be achieved for other non-body-of-revolution shapes.

The dashed lines in Fig. 9(*b*) display the percent difference values of the $L^* = 5$ results from Fig. 9(*a*). It shows that for nondimensional wavelengths greater than 1.5, the analytical solution slightly overpredicts the pitch moment on a square body by less than +5%. The figure also contains the results from the more slender, $L^* = 10$, geometry, shown as dotted lines in the figure. Our results appear to show that the analytical solution underpredicts the pitch moment on this body by less than −5%. The extremely shallow case with a nondimensional depth of 1.0 shows a slightly larger underprediction of −10% but this is not surprising considering that a wave-body interaction occurred on the square geometry at this depth as well.

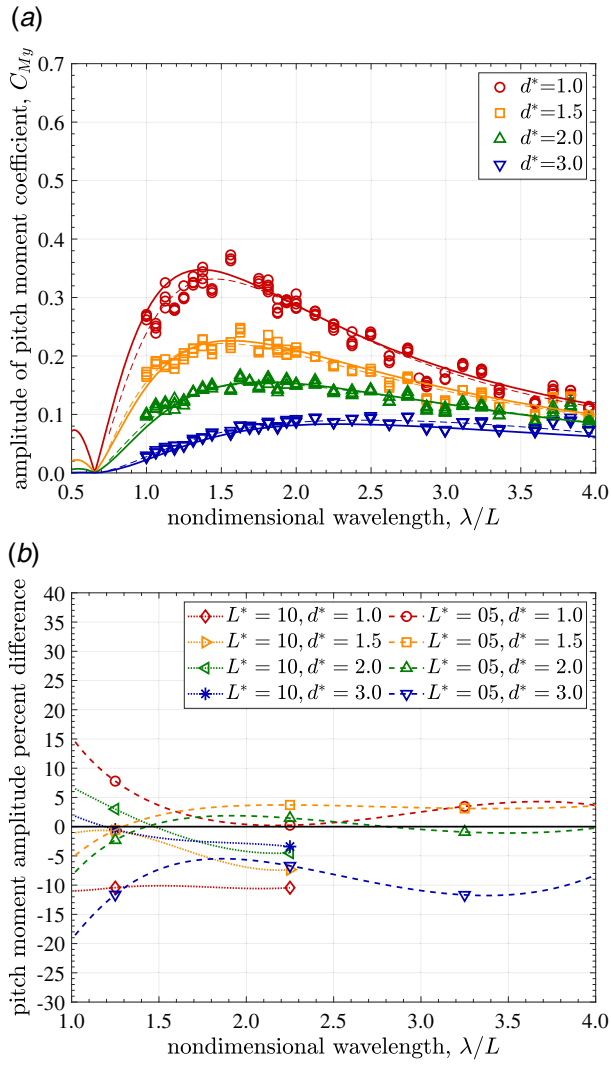

Fig. 9 Pitch moment amplitude comparison for the square body over a range of wavelengths, for two different body lengths, and four depths: (*a*) experimental and theoretical results for $L^* = 5$ body and (*b*) percent difference between theoretical and experimental results

5.3 End Face Curvature Assumption. Unlike the non-body-of-revolution square geometry, which the theory could not mathematically model, the theory can model a circular geometry with a flat end face. The analytical solutions for a flat-faced circular geometry are obtained by considering only the last row of terms in Eqs. (6) and (7) and setting α to 1. These new expressions for b_0 and a_1 allow us to create an analytical solution that mathematically captures the exact geometry and can be directly compared to experimental results from an identical geometry.

Figure 10(*a*) shows the percent difference of the heave force amplitude between the analytical solutions for this geometry and the experimentally measured results. The dotted line corresponds to the more slender, $L^* = 10$, geometry while the dashed line represents the less slender, $L^* = 5$, geometry. As nondimensional wavelength decreases below 1.5, the percent difference diverges rapidly as the heave force approaches a value of zero at a nondimensional wavelength of 1.0. However, for nondimensional wavelengths greater than 2.0, the analytical solution shows good agreement with the experimental results for the heave force. The percent difference is between −10% and +5% for these longer wavelengths. The extremely shallow depth case for both the more and less slender geometry showed a less accurate solution that underpredicted the heave force by around −15%.

These percent difference results are nearly identical to the ones previously shown in Fig. 4(*c*) for the circular geometry with hemispheric end caps. This shows that the heave force can still be well predicted by the analytical solution even if the end cap shape has high curvature, in violation of one of the assumptions of the theory.

Figure 10(*b*) displays the surge force amplitude percent difference of the flat end face analytical solutions relative to the experimental measurements. As in Fig. 10(*a*), the dashed and dotted lines capture the more slender and less slender geometries. For nondimensional wavelengths less than 1.5, the percent difference is rapidly diverging since the surge force equals zero at a nondimensional wavelength of 1.0 just like the heave force does. For nondimensional wavelengths greater than 1.5, however, the accuracy of the analytical solution is rapidly improving. For the less slender body, beyond nondimensional wavelengths of 2.5 or greater, the percent difference is less than ±5%. This is true for all four depths tested for this geometry. At nondimensional wavelengths around 2.0, the more slender body has a larger percent difference than the less slender body but it still appears to be decreasing. However, the exact percent difference value for longer wavelengths is not clear.

All of these trends for the surge force are, once again, nearly identical to the results for the circular geometry with hemispheric end

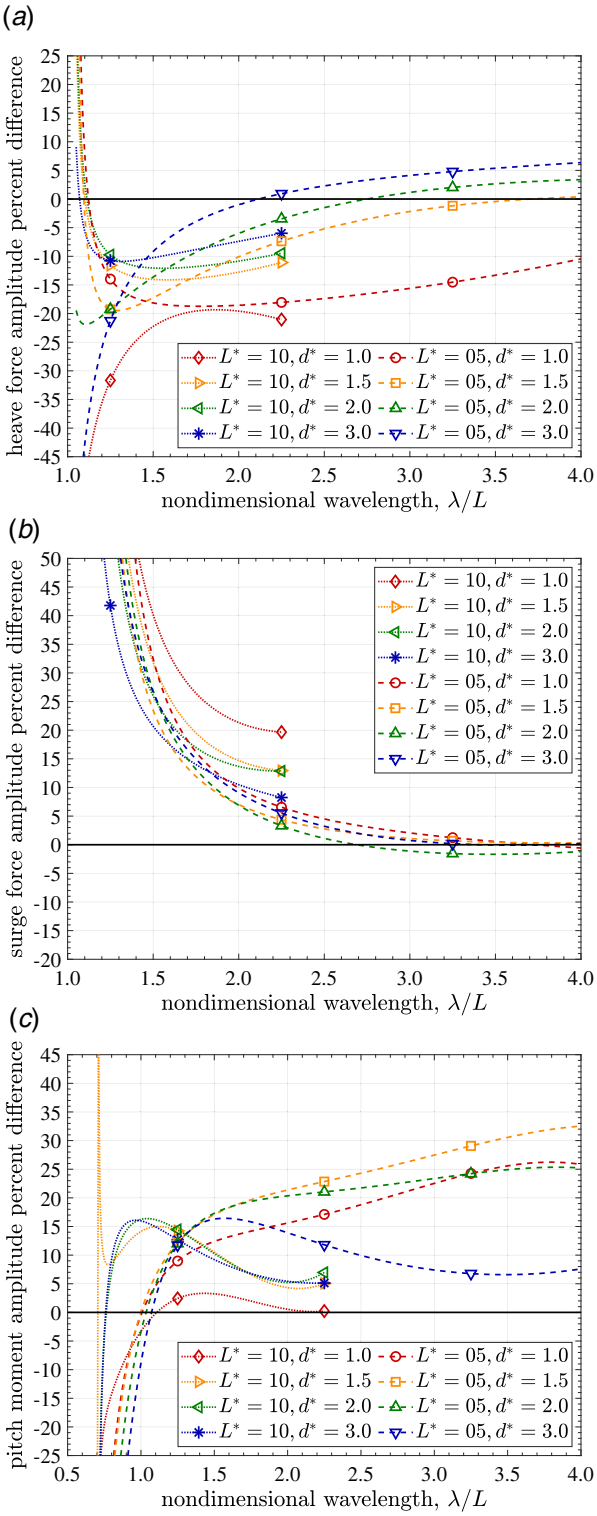

Fig. 10 Amplitude comparison of various loads for the circular body with flat end faces over a range of wavelengths, for two different body lengths, and four depths: (*a*) heave force amplitude results, (*b*) surge force amplitude results, and (c) pitch moment amplitude results

caps shown in Fig. 5(*c*). This suggests that, like the previously discussed heave force, the surge force can also be well predicted by the analytical solution regardless of the curvature of the end cap shape.

Figure 10(*c*) contains the pitch moment percent difference of the analytical solutions relative to the experimental results for a flat-faced geometry. The formatting is the same as Figs. 10(*a*) and 10(*b*) and again contains both the more and less slender geometry results. Since the pitch moment for this geometry goes to zero at a nondimensional wavelength of 0.70, the percent difference results quickly diverge for nondimensional wavelengths less than 1.0. For nondimensional wavelengths greater than 1.5, for the less slender geometry, the figure shows that the analytical solution overpredicts the pitch moment and the percent difference is between +20% and +30%. This is higher than the percent difference range for the circular geometry with hemispheric end caps shown previously in Fig. 5(*c*) which had a percent difference between +10% and +20%. Unfortunately, the more slender body percent difference result shows more fluctuations and therefore it is not possible to extrapolate the results out to longer wavelengths to access if the analytical solution is also less accurate for this geometry.

Although the analytical solution had good agreement with the experimentally measured heave and surge forces for a high-curvature end cap geometry, the pitch moment accuracy does appear to suffer. This could have potentially been expected, however, since the assumption regarding the necessity of a small curvature on the end caps in the theory was only required to perform the surface integration when doing the moment calculation. This explains why the accuracy of the heave and surge force predictions were unaffected by the infinite curvature of the flat end face but the pitch moment accuracy appears to be effected.

5.4 Phase Angle Sensitivity to Assumptions. To predict the heave force, surge force, and pitch moment time histories on a vehicle require knowledge of the phase of each load relative to the incoming wave. Figures 11(*a*)–11(*c*) show the relative phase of the heave force, surge force, and pitch moment, respectively, relative to the incoming wave for the more and less slender circular geometries with hemispheric end caps. Both body lengths are included together in the figures. The solid horizontal lines represent the theoretical values for the relative phases. These values do not depend on the slenderness of the body. The vertical lines represent the locations where the analytical solution predicts that the phase undergoes a jump discontinuity. These lines, on the other hand, do depend on the slenderness of the body. The vertical dotted lines represent the analytical solution for the more slender geometry while the vertical dashed lines represent the less slender geometry. Although not shown here, the theory also predicts that the end cap shape of the body will affect where the jump discontinuity will occur as well. The theory predicts that there is no dependence on the depth of the body.

For the circular cylinder with hemispheric end caps, the analytical solution predicted that the heave force will be in-phase with the incoming wave for nondimensional wavelengths between 0.45 and 0.90 for the more slender geometry and between 0.40 and 0.80 for the less slender one. Furthermore, the relative phase will be 180 deg out-of-phase for nondimensional wavelengths greater than those two ranges. For the flat face geometry, the theory predicts this transition to occur at a nondimensional wavelength of 1.0. The measured relative phase angles for the heave force, shown in Fig. 11(*a*), are in good agreement with the analytical solutions for all the depths and both the $L^* = 10$ and $L^* = 5$ geometries. The only disagreement with the theory is the smearing out of the sharp jump discontinuity. Since the jump discontinuity regions correspond to the minimum force location, this requires us to estimate the phase of an oscillating signal that has a very small amplitude. This results in a larger amount of uncertainty in the estimated phase in this region compared to the other regions.

The analytical solution for the surge force predicts that the surge force first leads by 90 deg and then trails by −90 deg. The nondimensional wavelength ranges that these values occur over, and the location of the phase jump discontinuities, are the same ones given previously for the heave force. The experimental results, shown in Fig. 11(*b*), agree well with the analytical solutions. The major difference from the analytical solution result is that the experimental results again show the phase jump appears to be centered

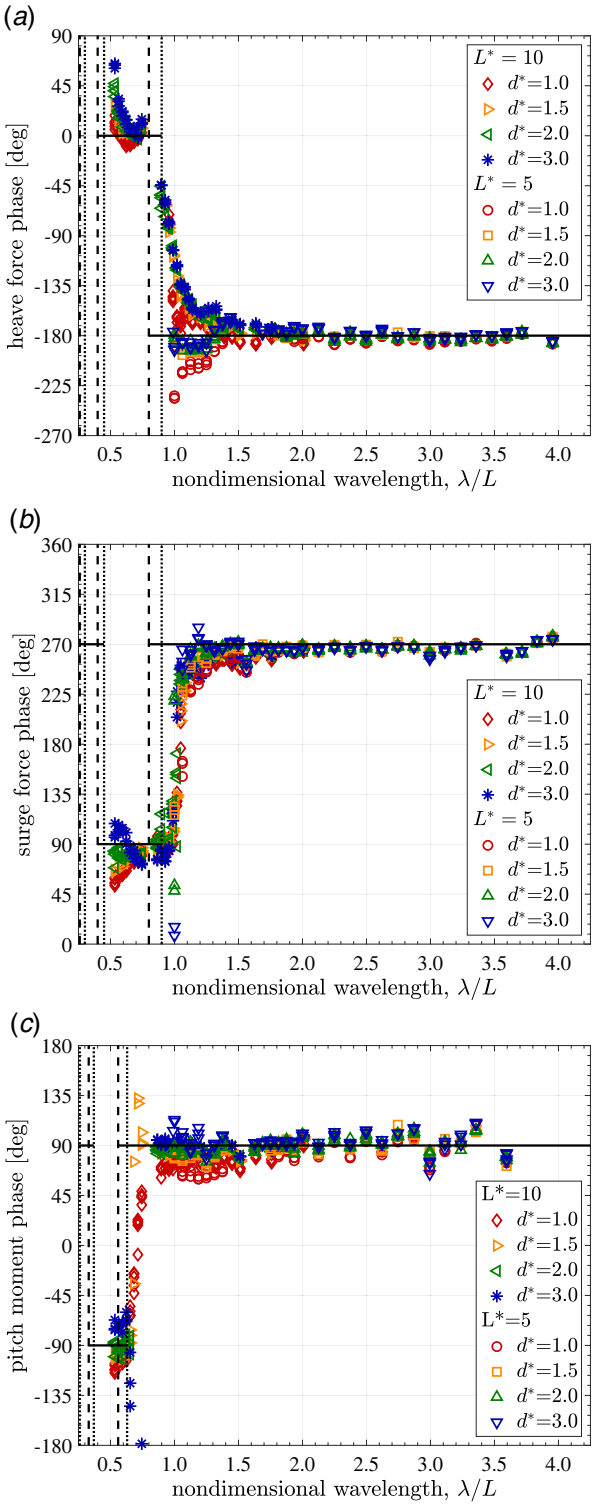

Fig. 11 Relative phase comparison of various loads for the circular body with hemispheric end caps over a range of wavelengths, for two different body lengths, and four depths: (*a*) heave force phase relative to incoming wave, (*b*) surge force phase relative to incoming wave, and (*c*) pitch moment phase relative to incoming wave

around a nondimensional wavelength of 1.0 and a smoothed out transition instead of a sharp jump.

For the pitch moment phase, the theory predicts that for nondimensional wavelengths between 0.37 and 0.63 for the $L^* = 10$ geometry and between 0.33 and 0.56 for the $L^* = 5$ geometry, the pitch moment phase trails the incoming wave by −90 deg. For nondimensional wavelengths greater than these, the phase leads the incoming wave by 90 deg. Figure 11(*c*) contains the comparison between the analytical solutions and the experimental measurements of the pitch moment phase relative to the incoming wave. The comparison shows that, again, the theory accurately predicts the relative phase. The experimental results show a jump discontinuity at a nondimensional wavelength slightly larger than 0.63 and the long wavelength asymptotic behavior of the phase is indeed to lead the incoming wave by 90 deg.

The same general behavior and overall accuracy of the theory shown in Figs. 11(*a*)–11(*c*) was also observed for the square non-body-of-revolution geometry and the flat face end cap geometry. Therefore, these additional results are not shown here. The results from these two geometries also contained a smeared out jump discontinuity where the phase switched for all three loads. Also, for both geometries, the heave and surge force experimental results appear to show the phase switch happening close to a nondimensional wavelength of 1.0 instead of the value of 0.9 or 0.8 predicted by the theory, depending on the geometry.

6 Conclusions

The analytical solution is able to accurately predict the wave-induced heave force when all the underlying assumptions are met and wavelengths are longer than the body length. For a slender, body-of-revolution geometry with a low-curvature end shape that is deeply submerged, the analytical solution is within ±5% of our experimentally measured heave forces for nondimensional wavelengths greater than 2.0. The deep-submergence assumption does not appear to be that restrictive as the theory showed this level of agreement even at a depth-to-diameter of 1.5. However, this value is specific to our testing conditions and is not universal. The actual depth where the assumption breaks down will depend on the size of the body and the wave height, as these two factors determine the amount of water between the hull and free surface. For our testing, $d^* = 1$ appeared to violate the assumption. Depth values that violate the assumption are important to identify because the theory is much less accurate in that case, underpredicting the heave force by −15%. The slender body assumption appears to not be a concern when considering the length-to-diameter ratios of typical torpedo-shaped UUVs. The analytical solution for the heave force agreed equally well with both our length-to-diameter 10 and 5 bodies. The end shape low-curvature assumption also appears to not be a concern as most typical UUVs have end shapes that are hemispheric. Even if the end shape has a higher curvature, our results suggest that the theory is still within ±5% of the experimental results provided it is deeply submerged. The body-of-revolution assumption, however, appears to be a more stringent requirement. This investigation found that modeling a square body using the circular cross-sectional analytical solution results in a disagreement with the experimental results that is depth dependent. The analytical solution underpredicted the heave force by −5% for $d^* = 3.0$, −20% to −10% for $d^* = 2.0$ and 1.5, and −25% for $d^* = 1.0$.

The analytical solution is also able to predict the wave-induced surge force accurately for wavelengths that are longer than the body length. When the theoretical assumptions are met, our results showed that the predicted surge force is within ±5% of our experimental measurements for nondimensional wavelengths greater than 2.0. The deeply submerged and low-curvature end shape assumptions appear to have no effect on the accuracy of the predictions. The body-of-revolution assumption appears to have a minor effect on the accuracy as the analytical solution underpredicted the surge force by −5% compared to the experimental results. The consequence of the slender body assumption is not as definitive. The results at the longest wavelength tested for the more slender body showed a larger percent difference than the less slender body. However, the percent difference was decreasing

and the analytical solution could eventually end up as accurate for longer wavelengths.

The analytical solution for the pitch moment has the least amount of accuracy. Even for the case where all the assumptions are met, the theory overpredicted the experimental results by +10% to +20% for nondimensional wavelengths greater than 2.0. The accuracy of the analytical solution does not depend on the depth of submergence, as long as the body is not operating very near the surface, nor on the slenderness of the body, over the two values tested. The assumption of a low-curvature end shape does affect the accuracy of the prediction and our results showed that a flat end face causes the analytical solution to overpredict the pitch moment from +20% to +30% percent for long wavelengths. The body-of-revolution assumption affects the accuracy of the solution as well but violation of the assumption appears to improve the accuracy of the prediction, at least for a square cross section.

For all three loads investigated, the analytical solution does an accurate job of predicting the phase angle of each load relative to the incoming wave. The only disagreement between the phase predictions and the experimental results is the location where the discontinuous phase jumps occur. The experiments appear to show that for all the cases tested, the forces transition around nondimenisonal wavelengths of 1.0 and the moment around 0.7, which disagrees with the theory for a circular cylinder with hemispheric end caps but does agree with the theory for a flat end face geometry. However, since in the experiments these jumps are smeared out over a small range of wavelengths, it is not possible to specify exactly when the phase transition occurs.

Acknowledgment

A preliminary analysis of the $L^* = 10$ geometry with hemispheric end cap results at two depths originally appeared in the Proceedings of the 37th International Conference on Ocean, Offshore, and Arctic Engineering as conference paper OMAE2018-77760. This article includes an updated analysis of that data and is expanded to include the rest of the depths tested and the other geometries used in a broader investigation. For the circular cylinder with hemispheric end caps, this involves two more depths and a second body with a different length-to-diameter. The broader investigation also included a square cross-sectional geometry and a circular geometry with flat face end caps.

The authors would like to thank Alison Kerr and the STEM summer internship program staff at the Naval Postgraduate School. C.Y. Cool's involvement was as a participant in the Naval Research Enterprise Internship Program (NREIP) sponsored by the Office of Naval Research (ONR). K.I. Yeager was involved over two summers, first as a participant in the Science and Engineering Apprenticeship Program (SEAP) sponsored by ONR, and then in the Research Participant Program sponsored by the Oak Ridge Institute for Science and Education (ORISE). The authors would also like to thank Barbara Berlitz for her assistance in proofreading the paper.

This work was supported by the Consortium for Robotics and Unmanned Systems Education and Research (CRUSER) project sponsored by the Department of the Navy, Office of Naval Research.

The views expressed in this paper are those of the authors and do not reflect the official policy or position of the Department of Defense or the U.S. Government.

Conflict of Interest

There are no conflicts of interest.

References

[1] Bingham, B., Agüero, C., McCarrin, M., Klamo, J., Malia, J., Allen, K., Lum, T., Rawson, M., and Waqar, R., 2019, "Toward Maritime Robotic Simulation in Gazebo," Oceans 2019 MTS/IEEE Seattle, Seattle, WA, IEEE, pp. 1–10.
[2] Ananthakrishnan, P., and Zhang, K. Q., 1998, "AUV Motion in a Wave Field," OCEANS '98 Conference Proceedings, Nice, France, IEEE, Vol. 2, pp. 1059–1063.
[3] Jones, L. M., Klamo, J. T., Kwon, Y. W., and Didoszak, J. M., 2018, "Numerical and Experimental Study of Wave-induced Load Effects on a Submerged Body Near the Surface," Proceedings of the 37th International Conference on Ocean, Offshore, and Arctic Engineering, Vol. 7B, ASME, Madrid, Spain, p. V07BT06A048.
[4] Carrica, P. M., Kim, Y., and Martin, J. E., 2018, "Near Surface Operation of a Generic Submarine in Calm Water and Waves," Proceedings of the 32nd Symposium on Naval Hydrodynamics, Hamburg, Germany, ONR.
[5] Carrica, P. M., Kim, Y., and Martin, J. E., 2019, "Near-Surface Self Propulsion of a Generic Submarine in Calm Water and Waves," Ocean Eng., **183**, pp. 87–105.
[6] Pinkster, J. A., 1981, "Mean and Low Frequency Wave Forces on Semi-Submersibles," Proceedings of the 13th Annual Offshore Technology Conference, Houston, TX, Offshore Technology Conference.
[7] Crook, T. P., 1994, September, "An Initial Assessment of Free Surface Effects on Submerged Bodies," Master's thesis, Naval Postgraduate School, Monterey, CA.
[8] Dean, W. R., 1948, "On the Reflexion of Surface Waves by a Submerged Circular Cylinder," Math. Proc. Cambridge Philos. Soc., **44**(4), pp. 483–491.
[9] Ursell, F., 1950, "Surface Waves on Deep Water in the Presence of a Submerged Circular Cylinder. I," Math. Proc. Cambridge Philos. Soc., **46**(1), pp. 141–152.
[10] Ursell, F., 1950, "Surface Waves on Deep Water in the Presence of a Submerged Circular Cylinder. II," Math. Proc. Cambridge Philos. Soc., **46**(1), pp. 153–158.
[11] Ogilvie, T. F., 1963, "First- and Second-order Forces on a Cylinder Submerged Under a Free Surface," J. Fluid. Mech., **16**(3), pp. 451–472.
[12] Arena, F., 1999, "Note on a Paper by Ogilvie: the Interaction Between Waves and a Submerged Horizontal Cylinder," J. Fluid. Mech., **394**, pp. 355–356.
[13] Cummins, W. E., 1954, "Hydrodynamic Forces and Moments Acting on a Slender Body of Revolution Moving Under a Regular Train of Waves," Technical Report 910, David Taylor Model Basin, West Bethesda, MD, December 1954.
[14] Newman, J. N., 1962, "The Exciting Forces on Fixed Bodies in Waves," J. Ship Res., **6**(3), pp. 10–17.
[15] Lee, C. M., and Newman, J. N., 1971, "The Vertical Mean Force and Moment of Submerged Bodies Under Waves," J. Ship Res., **15**(3), pp. 231–245.
[16] Wilmott, P., 1988, "On the Motion of a Slender Body Submerged Beneath Surface Waves," J. Ship Res., **32**(3), pp. 208–219.
[17] Cummins, W. E., 1954, "Forces and Moments Acting on a Submarine Moving Under Waves – Comparison of Theory With Experiments," Technical Report C-596, David Taylor Model Basin, West Bethesda, MD, December 1954.
[18] Henry, C. J., Martin, M., and Kaplan, P., 1961, "Wave Forces on Submerged Bodies," Tech. Rep. 808, Davidson Laboratory Stevens Institute of Technology, Hoboken, NJ, June 1961.
[19] Khalil, G. M., 2001, "Experimental Investigation of Wave Forces on Submerged Horizontal Cylinders," Indian J. Eng. Mater. Sci., **8**(2), pp. 59–65.
[20] Turner, T. M., Klamo, J. T., and Kwon, Y. W., 2018, "Comparison of Wave-Induced Loads on a Near Surface Slender Body From Inviscid Flow Linear Solution and An Experimental Model Test," Proceedings of the 37th International Conference on Ocean, Offshore, and Arctic Engineering, Vol. 7A, ASME, Madrid, Spain, p. V07AT06A015.
[21] Whitmer, A. R., Klamo, J. T., and Kwon, Y. W., 2019, "On the Validity of Predicting Wave-Induced Loads on a Submerged Body Using the Superposition of Regular Wave Results," Oceans 2019 MTS/IEEE Seattle, WA, IEEE, pp. 1–11.
[22] Klamo, J. T., Jones, L. M., Kwon, Y. W., and Didoszak, J. M., 2017, "Upgrades to and Current Research Efforts Involving the Tow Tank Facility at the Naval Postgraduate School," Proceedings of the 30th American Towing Tank Conference, SNAME, West Bethesda, MD.